



RESEARCH ARTICLE



Ultrasonic additive manufacturing of 4130 steel using Ni interlayers*

Chih-Hsiang Kuo^a, Niyanth Sridharan^b, Tianyang Han^c, Marcelo J. Dapino ^{oc} and S. S. Babu ^{oa,b}

^aThe University of Tennessee, Knoxville, TN, USA; ^b Materials science and technology division, Oak Ridge National Laboratory, Oak Ridge, TN, USA; ^cNSF IUCRC on Smart Vehicle Concepts, Department of Mechanical and Aerospace Engineering, The Ohio State University, Columbus, OH, USA

ABSTRACT

Ultrasonic additive manufacturing (UAM) is a solid-state manufacturing process for making complex components. However, fabrication of ferritic (body centered cubic) steels has been challenging for UAM due to its high hardness. This research successfully joined AISI 4130 steel sheets by using soft Ni (face centered cubic) interlayers. The localisation of plastic deformation in the Ni-interlayer leads to a significant reduction in voids. A post-process heat-treatment was designed using thermodynamic calculations to dissolve nickel into steel matrix. Energy dispersive X-ray spectroscopy measurements showed $\sim 10~\mu m$ Ni from the interlayer diffused into the steel side, confirming the feasibility of the approach. The shear tests show a higher shear strength in comparison to as-processed 4130 without interlayers and post processed using hot isostatic pressing (HIP).

ARTICLE HISTORY

Received 14 December 2018 Revised 31 March 2019 Accepted 8 April 2019

KEYWORDS

4130 steel; Ni interlayers; solid-state welding; shear testing; microstructural characterisation

Introduction

Manufacturing steel with solid-state welding techniques such as explosive welding and friction stir welding have been/are being established [1,2]. However, it is often challenging to fabricate complex geometries with common solid-state techniques. Using ultrasonic additive manufacturing (UAM), it is possible to fabricate parts with complex geometries and embed fibre optic strain gauges. UAM is an advanced solid-state manufacturing process that utilises a sonotrode that vibrates at a 20 kHz frequency with an amplitude of 20-50 µm generating plastic deformation and obtaining metallic bonding at the nascent plane between foils [3-7]. To achieve bonding in UAM, plastic deformation is necessary [8-10]. However, the high strength of the steel necessitates larger power input leading to rapid tool wear and nugetting [11]. Therefore only soft materials such as Al [4, 12-14] and Cu [15,16] alloys have been successfully manufactured using UAM, while only limited literature about UAM with steels has been reported [11].

Owing to the limited amount of published literature on fabricating steels through UAM, the authors reviewed other solid-state joining processes, i.e. friction and friction stir welding with high strain rates similar to UAM [2,17,18] for guidance to the current research. This review indicated crucial differences between UAM

and other solid-state joining processes. For instance, in the case of friction welding and friction stir welding of steels, the temperature rise can heat up the steel closer to Ac₁ or Ac₃ temperature, which would lead to austenitisation in the stir zone [2,18], and thereby enabling plastic deformation in the joint zone. Yet, it has been shown that all steels do not necessarily austenitise during friction stir welding. The alloys which are lean in carbon tend to have higher Ac1 temperatures and are also soft. The softness would result in lower peak temperatures due to the lower energy input required to weld these steels. The lower energy input could benefit the welding process by preventing nuggets and rapid tool wear [2], which are some of the major challenges in welding steels using friction welding. Interestingly, UAM has a modest macroscopic temperature increase [19] in materials, which supports the reason for poor joining characteristics. Based on the above review, we could conclude that UAM of steels can be successful only if the initial zone undergoing plastic deformation is either soft originally or achieves the soft state during processing (above the Ac₃ in the γ region).

One way to circumvent this challenge would be to use soft interlayers in between the steel layers. There are studies on soft-hard dissimilar metal combinations in UAM such as steel-tantalum [3], steel-aluminium [20,21], titanium-aluminium [5,7], and

CONTACT Niyanth Sridharan niyanth.sridharan@gmail.com

*This article has been authored by UT-Battelle, LLC under Contract No. DE-AC05-000R22725 with the U.S. Department of Energy. The United States Government retains and the publisher, by accepting the article for publication, acknowledges that the United States Government retains a non-exclusive, paid-up, irrevocable, world-wide license to publish or reproduce the published form of this article, or allow others to do so, for United States Government purposes. The Department of Energy will provide public access to these results of federally sponsored research in accordance with the DOE Public Access Plan (http://energy.gov/downloads/doe-public-access-plan).

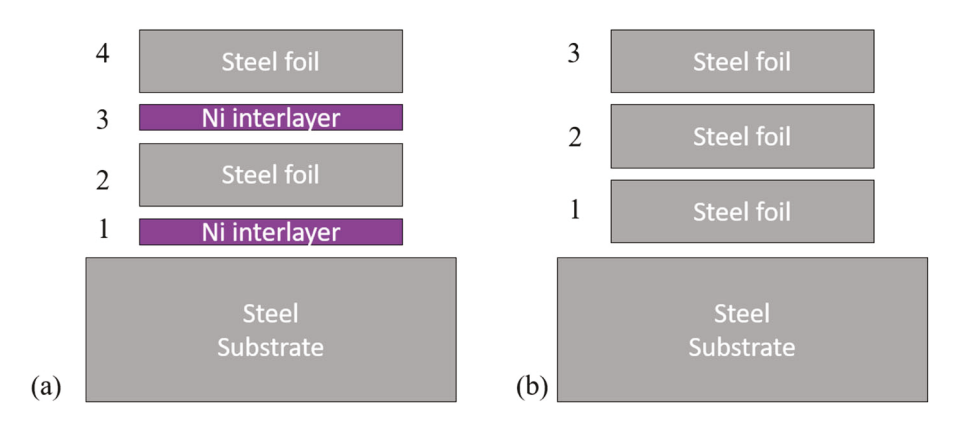


Figure 1. Schematic of welding sequence of 4130 (a) with Ni interlayer (b) without Ni interlayer.

Table 1. Nominal composition in percentage (%) of 4130 and Ni 200.

Element	Cr	Mn	С	Si	Мо	S	Р	Ni	Cu	Fe
4130 Ni 200	0.9	0.5 0.35	0.29 0.02	0.2 0.35	0.2	0.04 0.01	0.035	– Balance	_ 0.25	Balance 0.4

copper-aluminium [16]. Most of the plastic deformation occurred in the softer materials and resulted in the formation of metallurgical bonding [20]. In addition, if the soft interlayer can be dissolved into steel foil by post weld heat-treatment (PWHT), a steel to steel weld can be achieved. The next design criterion is reducing the tendency for the formation of liquid phase and brittle intermetallic compounds during processing or PWHT. Therefore, the selection of an interlayer material should be based on (1) low hardness, (2) higher melting point than processing temperatures, (3) reduced intermetallic formation susceptibility during PWHT and (4) ability to dissolve into steel, i.e. increased solid solubility in the matrix phase. With a quick review of (Fe-X) binary phase diagrams with many alloying additions (X), one can conclude that nickel is a potential interlayer candidate. Since nickel has good solubility in body centered cubic (BCC)-Ferrite (>3 wt-%) and in face centered cubic (FCC)-Austenite (isomorphous), a single-phase solid solution can be achieved by using suitable PWHT (temperature and time). The major challenge for Ni-Fe inter diffusion is the correct selection of temperature for PWHT. While higher temperatures lead to enhanced diffusion, an increase in temperature above Ac3 would lead to a drop of diffusivity of Ni in steel matrix due to the allotropic transformation of BCC to FCC [22, 23]. Moreover, higher temperature conditions may also lead to the formation of Kirkendall voids due to the significant difference in intrinsic diffusivity of Ni and Fe at the Ni-steel interface, which lowers the bond strength.

Therefore, this research will evaluate the feasibility of using Ni as an interlayer both from a perspective of UAM and post-processing treatments to facilitate the fabrication of 4130 steel parts using UAM. Thus, low alloy 4130 steel tapes (120 µm) were processed using high purity Ni 201 tapes as the interlayer. The asfabricated builds were heat-treated to dissolve the Ni into the 4130 foils in the solid state. Shear tests were

Table 2. Weld parameters used for steel-Ni build.

Parameter	Level
Weld force (N)	9000
Weld speed (mm/s)	33.87
Amplitude (µm)	37.87
Temperature (°C)	93.33

conducted on both the as-fabricated and post-weld heat-treated conditions to evaluate the performance.

Experimental details

Sample Fabrication

In this study, five layers of 0.127 mm (0.005 in) thick annealed 4130 steel foils and five layers of 0.025 mm (0.001 in) thick Ni 201 foils were alternatively welded onto a 5.08 mm (0.2 in) thick annealed 4130 baseplate (see Figure 1). The nominal compositions of 4130 steel and Ni 201 are presented in Table 1. A bilayer arrangement where steel is laid on top of Ni is used. This technique has been used in the past to fabricate Al-Ti builds and these details are discussed elsewhere [5]. Pilot welds were performed to determine a viable set of weld parameters. For the sake of comparison another set of builds without any interlayers were also fabricated. Using the same weld parameters, the average power drawn is close to 3250 W to weld the steel with Ni interlayer while 4200 W power was used to weld the 4130-4130 baseplate [11]. Selected parameters for making all the samples in this study are shown in Table 2. This set of parameters is not formally optimised.

Thermodynamic calculations

To optimise the post processing treatments without the time-consuming trial and error process, interdiffusion calculations using $x = \sqrt{D}t$ (x is inter diffusion

distance, D temperature dependent diffusion coefficient and *t* is time) were performed to down select the ideal temperature to maximise Ni inter diffusion. Following this, THERMOCALC® and DICTRA® [24,25] software were used to simulate the post weld heat treatments. The simulation was initialised as a 25 µm thick Ni sheet attached to a 125 μm thick sheet of steel. These values correspond to the actual dimensions of the foils used for consolidation of the samples. Simulations were performed at 1000 K (identified using analytical diffusion calculations method) for 1, 2, and 10h to evaluate the inter-diffusion of Ni with steel. The Ac₁, Ac₃, and M_s temperatures of the steel matrix were calculated by JMatPro[®] with varying Ni wt-% to understand the role of nickel uptake.

Post weld heat treatments

Following the simulations, post weld heat treatments were performed at 1000 K for 1, 2, and 10h to validate the simulations. The actual heat treatment was conducted in vacuum at a heating rate of 30°C min⁻¹ and a cooling rate of less than 10°C min⁻¹. Following heat treatment, cross-sections were prepared for detailed microscopy to evaluate the extent of diffusion of Ni into the steel and the microstructure evolution.

Microstructure characterisation

The cross-sections were polished using standard metallographic techniques and then etched using a 2% Nital solution. The cross-sections were then characterised using optical microscopy, scanning electron microscopy, energy dispersive spectroscopy and electron backscatter diffraction to understand the effect of Ni diffusion on the microstructure. Electron microscopy was performed using a JEOL 6500 F equipped with an energy dispersive X-ray spectroscopy (EDS) detector and an electron backscatter diffraction detector. The imaging and electron backscatter diffraction (EBSD) were performed at an accelerating voltage of 20 kV and a probe current of 2 nA was used. Local mechanical properties were characterised using nanoindentation to understand the effects of the weld fabrication using interlayers using a Nanomechanics Inc. iMicro system with InForce 1000 actuator. A threefaced Berkovich indenter was applied to a displacement of 500 nm at a strain rate of 0.05 s^{-1} with a dwell time of 20 s to remove time-dependent plasticity effects. The indents were placed with a spacing of 10 µm. The load displacement curves were analysed using the Oliver Pharr technique [26].

Mechanical testing

Shear testing was conducted to obtain mechanical strength of the weld interface. Three shear specimens

of each heat-treatment condition were cut out from UAM samples. Details of this method are discussed elsewhere [5,11]. The as-welded and samples post processed at 1000 K for 1 and 10h were tested. The nominal dimensions of the shear specimens are $4.95 \times 4.83 \times 3.81 \text{ mm}^3$ and shown in refs. [5,11]. Specimens were tested using a 50 kN MTS load frame where the load was applied until failure.

Results and discussions

Characterisation of the as-fabricated samples

The as-received microstructure of 4130 steel foils had martensite + carbide microstructure. However, a softening step was essential to enable plastic deformation in the steel to allow for joining without interlayers. With such pre-processing, the as-received foil and plate microstructure contained a microstructure of ferrite + tempered martensite + carbides. Figure 2 shows the 4130 steel interfaces processed without nickel interlayer at different length scales and shows varying degrees of bonding. The optical micrograph (Figure 2(a)) shows the presence of voids in the interface. Figure 2(b) shows the voids (marked with a red box) at higher magnification and confirmed the lack of plastic deformation. Interestingly, the bonded zones shown in Figure 2(c) show plastic flow. The evidence for the plastic deformation [see Figure 2(d)] is inferred from the decomposition of cementite (Fe₃C) laths near the interface. Although the dissolution of pearlite in steels and supersaturation of ferritic matrix due to heavy plastic deformation has been extensively documented in the past [27,28], the onset of such mechanisms during UAM is not proven and requires future work with site-specific atom probe tomography measurements.

In the next step, the as-received 4130 foils without any softening heat treatments were bonded with nickel interlayers. Interestingly, good welds were produced without the need for annealing treatments of steel foils. The SEM micrographs from this configuration are shown in figure-3 (a-c). Figure-3 (a) shows two interfaces at a low magnification. The micrograph clearly shows significant reduction in the number of voids, as well as, non-uniform grain refinement. The refinement is more pronounced in the region where the Ni flows along the contours of the steel, i.e. where the steel surface is rough (region is marked in Figure 3(a)). The flat interfaces, on the other hand, (marked in Figure 3(c)) does not show significant refinement. Higher magnification images of the regions marked in Figure 3(a) and (c) are shown in Figure 3(b) and (d) respectively, which clearly contrast the difference in the refinement of the grains. This has been previously observed during welding Al-Ti dissimilar metal welds [5,7] and steel-Ta dissimilar metal welds [3]. The roughness in the

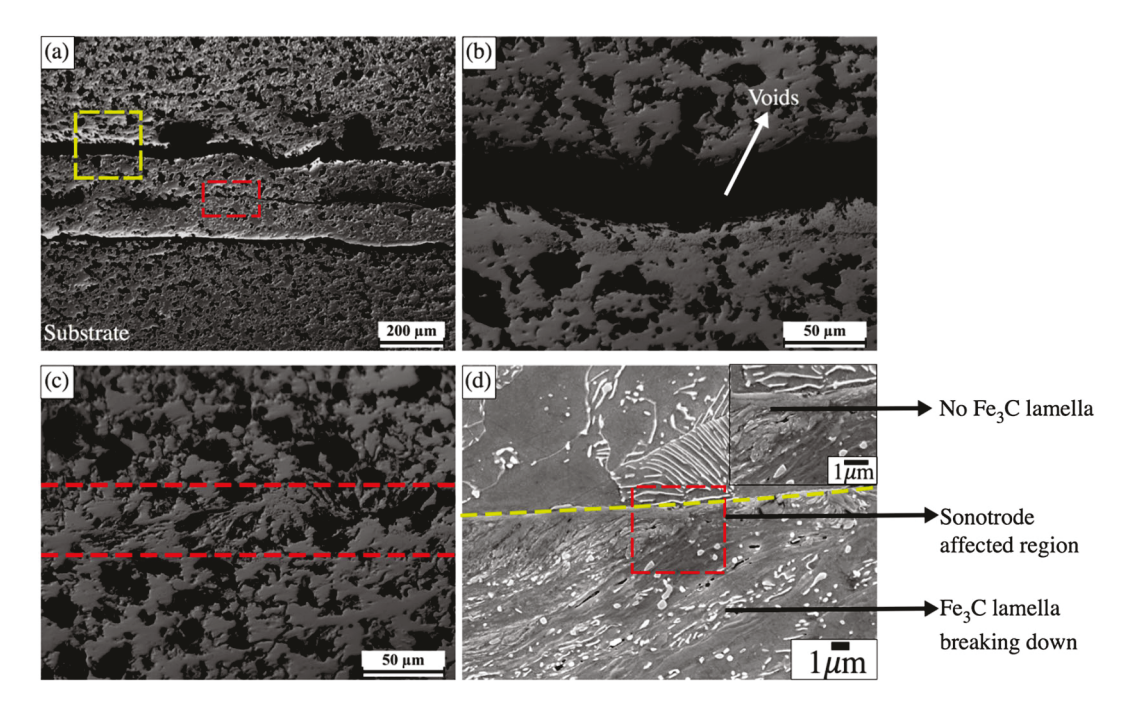


Figure 2. 4130 Steel-Steel in the as welded without interlayer (a) optical micrograph showing significant void fraction and the heterogeneity in the interface (b) Optical micrograph showing the un bonded regions (c) Optical micrograph of the bonded location (d) SEM image of the interface corresponding to the bonded region shown in figure (c) and the inset shows the possibility of localised cementite lamella dissolution.

upper portion of the foil is induced by the sonotrode during the welding of the previous foil. This plastic deformation from the sonotrode results in grain refinement only in the upper surface of the steel foil as observed previously with Al and Ti dissimilar metal welds. This sonotrode affected region results in Ni flow into the contours and consequently generate the wave

formation as seen in Figure 3(b). Owing to this lack of plastic deformation at the bottom foil, the bottom foil should therefore have a lower hardness compared to the sonotrode affected regions. In addition, due to the concentration of plastic deformation in Ni as hypothesised the difference in the hardness gradients should also be significant.

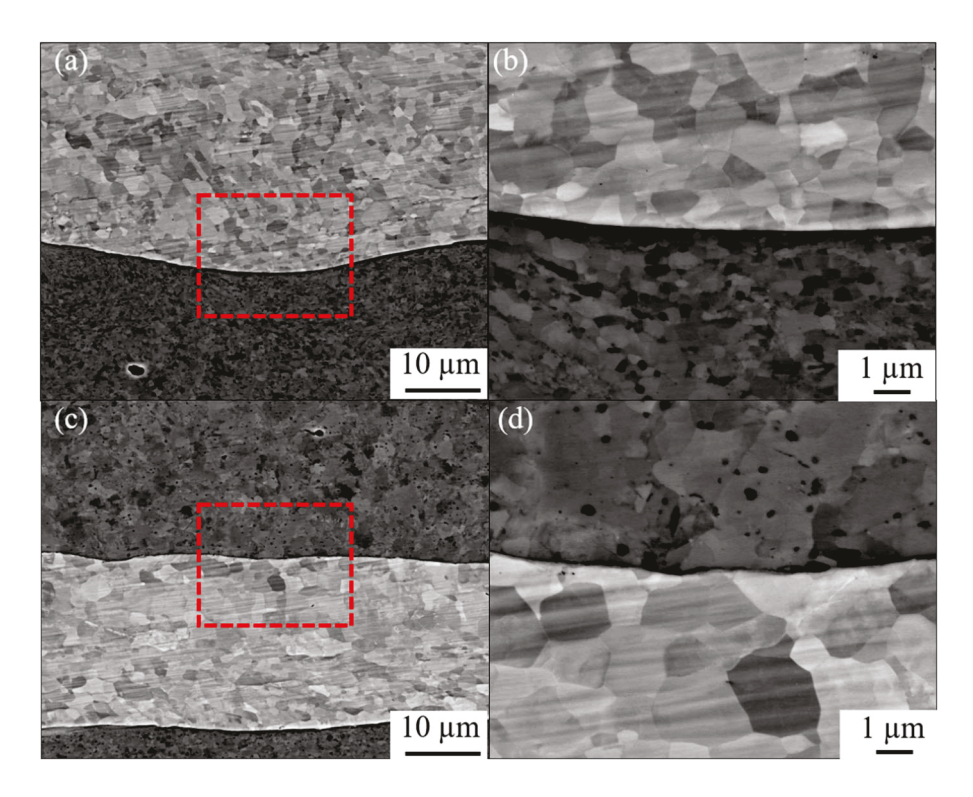


Figure 3. 4130 Steel-Ni-Steel in the as welded condition (a) & (b) SEM-back scatter image showing the grain structure in Ni and steel in a region where Ni flows into the contours of the sonotrode affected region (c) & (d) SEM-back scatter image showing the grain structure in Ni and steel in a region with a flat interface showing deformation concentrated in the Ni foil zzzz.

To confirm local differences in the mechanical properties detailed nano indentation was performed. The hardness measurements were primarily aimed at understanding the effects of localised plastic deformation at the interface. Nano-indentation results show that upper surface of the foil (sonotrode affected region) has higher hardness compared to the lower surface of the foil. Higher hardness was measured in the region located within the sonotrode affected in the upper surface of the foil $(5.76 \pm 0.41 \text{ GPa})$, compared to region lower surface of the foil $(4.24 \pm 0.12 \text{ GPa})$. The hardness of Ni interlayer is 3.53 ± 0.08 GPa. However, in the case of steel to steel welds fabricated without any interlayer the hardness at the interface is 6.5 ± 0.27 GPa. This could be attributed to the higher energies used for fabricating the steel to steel builds. The result of such increases in power is manifested in the interface.

To study the local effects deformation with the addition of Ni interlayer detailed electron backscatter diffraction was performed. The results are presented in Figure 4(a,b). Figure 4(a) shows the inverse pole figure (IPF) corresponding to the samples fabricated with a Ni interlayer. The EBSD micrographs clearly show the difference in the grain structure at the interface. For instance, the ferrite grains in the steel samples fabricated without interlayers are much finer compared to the samples fabricated with an interlayer. This reduction in grain size for the samples fabricated without the interlayers could have resulted due to the higher UAM power used to fabricate these builds. A higher power implies higher plastic deformation. A more detailed texture analysis needs to be performed to rationalise the relationship between the applied power and the plastic deformation at the interface which is beyond the scope of this paper.

Post weld heat treatment simulations

The purpose of the post weld heat treatment simulations was to identify process parameters to enable Ni dissolution into the steel in the solid state without timeconsuming trial and error. The aim of performing such calculations is to select the temperature which would maximise Ni dissolution in the steel at the minimum

time. A preliminary review of the inter diffusion of Ni in steel suggests that the maximum diffusion coefficient is below the lower critical temperature. This is due to the formation of FCC above the Ac1 which leads to a reduction in the diffusion coefficient. The diffusion coefficient of Ni in BCC is two orders of magnitude higher than in FCC. The changes in the diffusion coefficient as a function of temperature can be estimated using the following analytical equations reported elsewhere [22,23].

$$D_{\nu} = 0.77e^{\left(\frac{-67,000}{RT}\right)} \tag{1}$$

$$D_{\alpha,T>800^{\circ}C} = 1.3e^{\left(\frac{-56,000}{RT}\right)} \tag{2}$$

$$D_{\alpha,680^{\circ}C < T \le 800^{\circ}C} = 1.4e^{\left(\frac{-58,700}{RT}\right)}$$
 (3)

The results are shown in Figure 5(a). The calculations based on the classical diffusion equation $x = \sqrt{Dt}$ show that for a 10-hour treatment at 800°C (1073 K) the maximum achievable inter diffusion zone is ~ 15 μm. The preliminary calculations also indicate that for a given time inter diffusion of Ni into steel is maximised at 800°C (1073 K) [23]. Based on these preliminary calculations DICTRA was used to calculate the extent of inter-diffusion of Ni into the steel at 1000 K with different holding times [25]. The results are presented in Figure 5(b). The results from the DICTRA simulations however are significantly different from those results calculated based on the analytical diffusion model. The data clearly shows that only a maximum of 6.5 µm of Ni could be dissolved into the steel. This discrepancy can be rationalised as follows. The post-weld heat treatment was conducted at 1000 K, which is below the lower critical temperature of 4130 steel, therefore, no ferrite to austenite phase transformation was originally expected. However, upon heat treatment the inter-diffusion of Ni into the steel effects a reduction in the lower critical temperature increasing the localised formation of an FCC layer. As stated previously formation of an FCC layer leads to the significant reduction in the diffusion coefficient. Calculations using JMatPro® showed that with the addition of Ni to 4 wt-% into 4130 steel, Ac3 is lowered from 1072 to 995 K, which is lower than the heat treatment temperature 1000 K which leads to

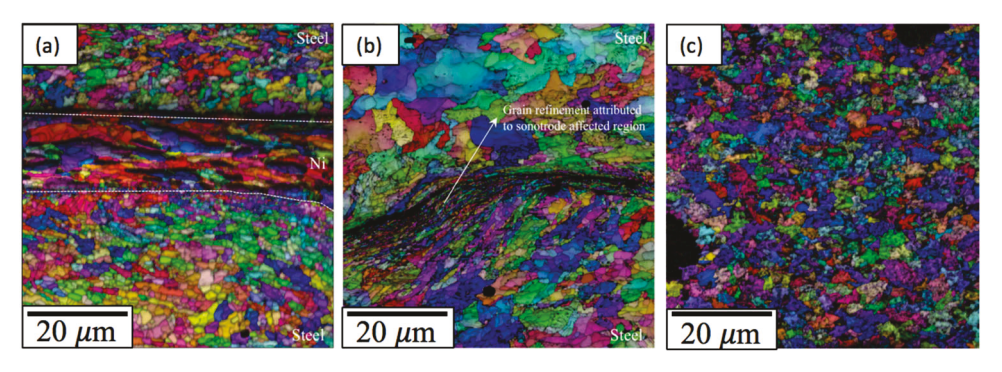


Figure 4. Inverse pole figure of the (a) steel to steel weld with a Ni interlayer, and (b) steel to steel build without any interlayer (c) as received foil.

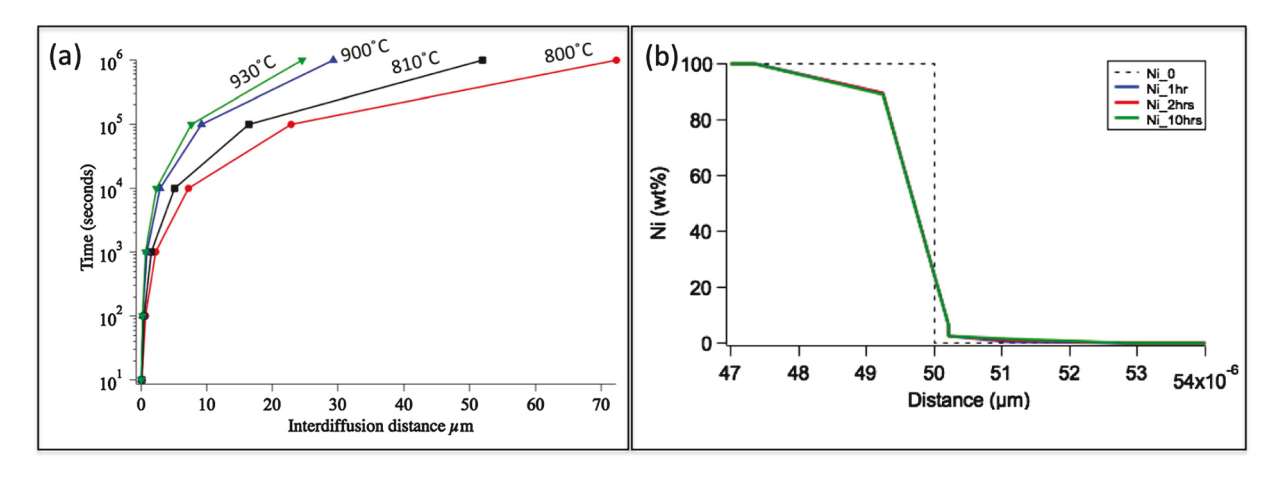


Figure 5. Calculated inter diffusion distances (a) using analytical $(x = \sqrt{Dt})$ equation to calculate the inter-diffusion distance (b) using DICTRA.

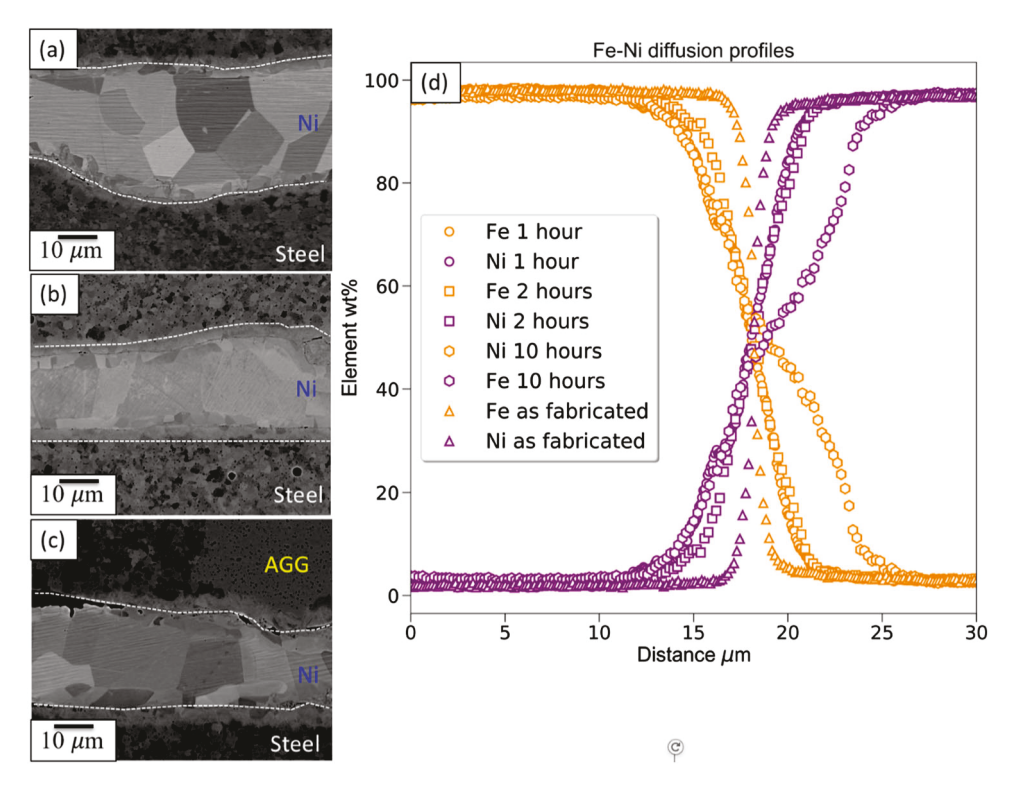


Figure 6. SEM BSE images showing the interfaces after heat treatment at 1000 K (a) 1 h (b) 2 h and (c) 10 h (d) EDS line scans clearly showing the extent of inter diffusion of Fe (purple) and Ni (orange) in the as processed and post processed samples. AGG: abnormal grain growth.

the formation of austenite. While the analytical calculations are unable to account for these transformations, DICTRA accounts for these. To investigate the effect of post-processing the samples fabricated with Ni interlayers were then subject to heat treatment at 1000 K for 1, 2 and 10 h and analysed. The results are presented in the following section.

Characterisation of post weld heat treated interfaces

The micrographs of the heat-treated and as-welded samples for comparison are presented in Figure 6. Figure 6(a-c) shows the microstructure after heat treatment of 1000 K for 1, 2 and 10 h, respectively.

The SEM-BSE micrographs show contrast at the Ni–Fe interfaces, which is evidence of inter-diffusion of Ni in steel. In addition, there is a zone in the steel adjacent to the Ni foil showing different contrast which is attributed to the formation of FCC layer. While significant grain growth in the Ni foils occurred during the annealing treatment, the grain growth in the case of FCC zone was limited. In addition, the grain growth did not occur in the steel foils as well in the case of the samples annealed for 1 and 2 h while abnormal grain growth (marked in Figure 6(c)) did occur in the samples subject to the 10-hour heat treatment. The reason for this apparent difference in the grain growth is beyond the scope of the paper and more work is warranted to study these phenomena in more detail. The extent of inter

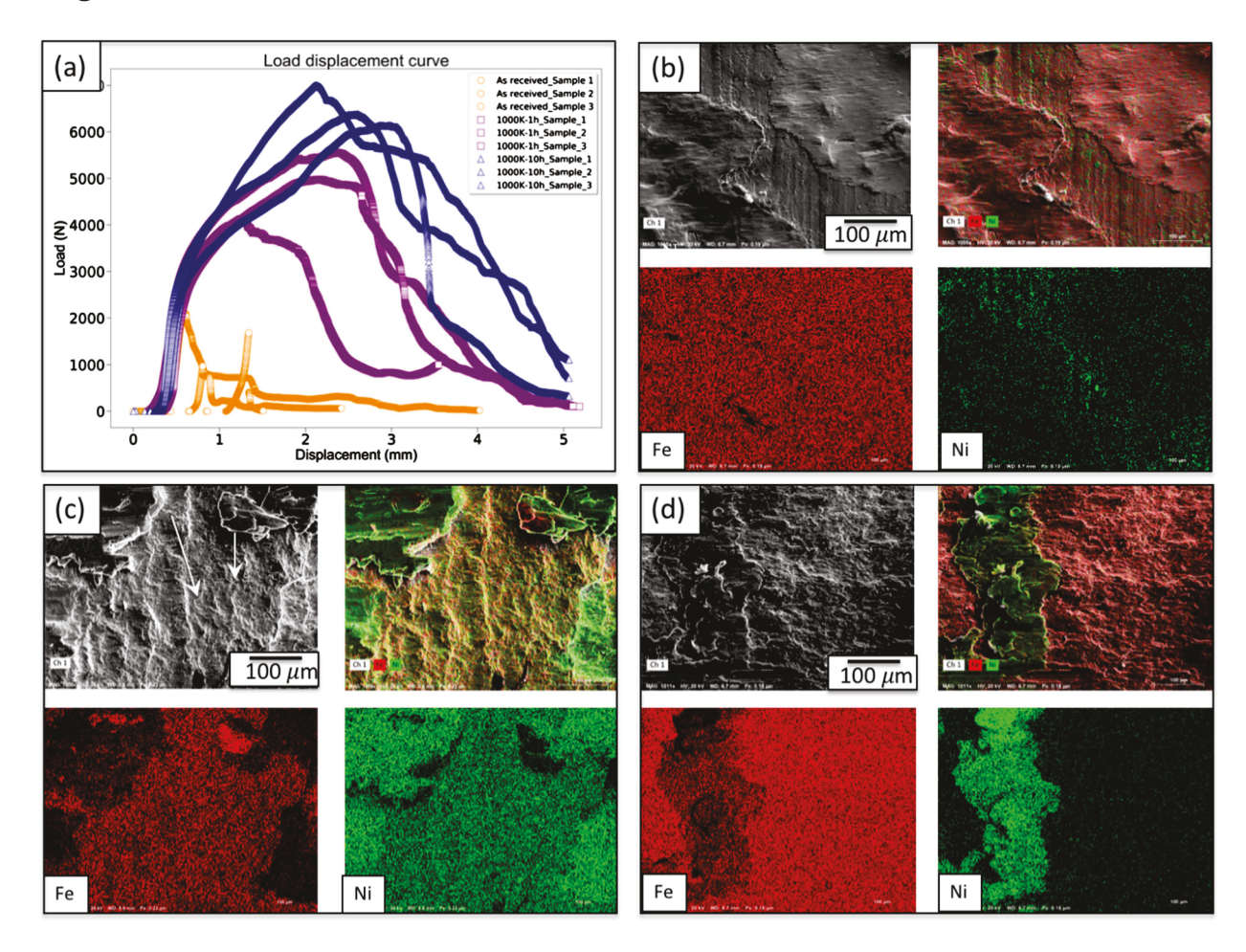


Figure 7. (a) Load vs. displacement curves for shear testing of the as processed and the heat-treated specimens (b) examination of the fracture surface of the as fabricated sample (c) examination of the fracture surface of the sample post-processed at 1000 K for 1h (d) examination of the fracture surface of the sample post-processed at 1000 K for 10h.

Table 3. Summary of the shear test results.

		Area unde	er the curve (N	mm)	
	Test-1	Test-2	Test-3	Mean	Coefficient of variation
As fabricated	1468.65	276.4846	141.67	628.93	1.16
1000 K 1 h	29,082.00	12,444.00	7389.00	16,305.00	0.67
1000 K 10 h	21,210.00	19,581.00	16,062.19	18,951.06	0.14
		Max	imum load (N)		
	Test-1	Test-2	Test-3	Mean	Standard deviation
As fabricated	2119.776	970.862	1680.425	1590.354	0.239
1000 K 1 h	5567.083	4981.636	4139.923	4896.923	0.113
1000 K 10 h	7004.251	6380.572	6141.53	6508.784	0.064

diffusion is measured using EDS. EDS measurements corresponding to each condition is shown adjacent to the micrograph and is plotted in Figure 6(d). The EDS micrographs show an inter diffusion zone $\sim 10~\mu m$ which is close to the DICTRA simulations. This clearly shows that having Ni interlayers with thicknesses < 10 um would completely dissolve in the steel leading to the formation of a steel-steel interface as hypothesised in the previous section.

Mechanical testing and fracture surface characterisation

The load vs. displacement curves obtained during shear testing of 4130 steel with Ni interlayers in the as-welded

and PWHT conditions are shown in Figure 7. The results are tabulated in Table 3. As expected, the shear strength and area under the load-displacement curves (total energy absorbed) are maximised for the condition where the samples are annealed for 1000 K for 10 h and decreases with a decrease in the annealing temperature. The results show that after PWHT for 10 h, the shear strength increased more than three times relative to the as-welded condition. Apart from an increase in both the maximum load and the area under the curve, longer heat treatment times also reduce the heterogeneity in the mechanical properties as evidenced by the standard deviation values shown in Table 3.

Follow up characterisation was performed on the shear fracture surface to understand the reason for

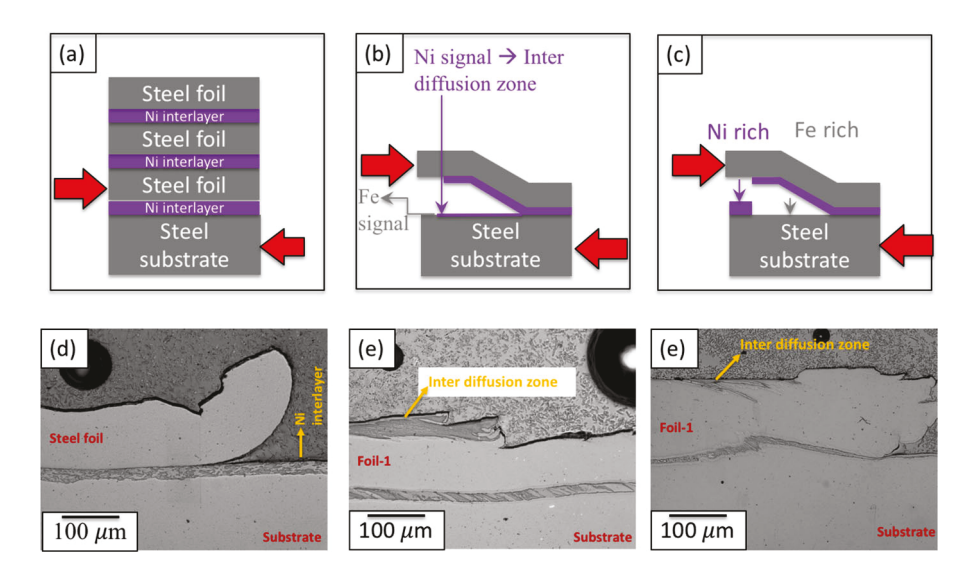


Figure 8. (a) Schematic illustration of the shear test geometry (b) schematic illustration of the fracture morphology of the sample post processed at 1000 K for 1 h (c) schematic illustration of the fracture morphology of the sample post processed at 1000 K for 10 h (d) optical micrograph of the fractured samples of the (a) as fabricated sample showing fracture occurred by delamination of the first layer (b) post processed for 1 h showing fracture occurring via multiple layers (c) post processed for 10 h showing fracture occurring via multiple layers as illustrated in Figure 8(c).

the improvement in strength and absorbed energy of the heat-treated samples. The results are presented in Figure 7(b,c). Figure 7 (b) corresponds to the samples heat treated for 1 h while Figure 7(c) corresponds to the samples heat treated for 10 h. The respective EDS maps indicate the presence of both Fe and Ni-rich regions along the entire fracture surface indicative of fracture occurring across multiple layers. While Figure 7(b) shows the presence of both Ni and Fe along the entire fracture surface, the Fe and Ni distribution in the case of samples heated for 10 h are discrete with local Fe and Ni-rich regions. This could be attributed to the location of the fracture. For instance, the presence of both Fe and Ni in the sample post-processed for 1 h is indicative of fracture occurring in the inter-diffusion zone while the sample post-processed for 10 h is indicative of fracture in the steel. A schematic illustration of the fracture methodology is shown in Figure 8(a-c). Figure 8(a) shows a schematic illustration of test geometry. Figure 8(b) shows the failure morphology for in the case of the sample post processed at 1000 K for 1 h, while Figure 8(c) shows the failure morphology in the case of the sample post processed at 1000 K for 1 h. The fracture morphologies are interesting, because the extended heat treatments allowed the steel matrix to absorb the energy due to loading by co-deforming with nickel enriched regions. This design philosophy can be used for complex UAM geometries.

The average maximum shear load for UAM 4130-4130 steel welds were tested using the same technique in a previous study and reported to be 1690 N for the as processed state and 4921 N after a post processing treatment using spark plasma sintering [11]. While using the Ni interlayer in the as fabricated state the mean load was 1590 N and upon post processing using a simple heat treatment cycle for one hour an average maximum load of 4896 N was achieved. Significant improvements were achieved via a 10-hour treatment which showed an average maximum load of 6508 N. However, optimising the Ni-interlayer thickness to achieve complete inter diffusion of Ni in the future needs to be performed.

Published literature on both similar and dissimilar metal welds have shown an improvement in both the strength and elongation during post processing [5,12,13,16]. While it has been shown that in the case of dissimilar metal welds the formation of a thin layer of intermetallic acts similar to a thin braze layer [16]. Consequently, the biaxial stress state achieved leads to improvement of mechanical strength [16] although significant void closure does not occur. This has been reported in Al-Cu and Al-Ti samples. In this case, as well a small layer of FCC region is present at the interface. The role of the FCC layer on plastic deformation is still not clear and is a matter of future investigation.

Summary and conclusions

A design and manufacturing methodology for 4130 steel builds using UAM with Ni interlayer was demonstrated with a reduction of ultrasonic energy by 50%. The selection of nickel and post processing treatments were designed using computational thermodynamics and kinetics tools to achieve solid-state dissolution. The nickel layer allowed for (i) sustained plastic deformation at abetting interfaces, (ii) eliminated intermetallic phase formation and (iii) enabling solid-state dissolution into the steel matrix (up to 10 µm into steel matrix) during post weld heat treatment. The shear tests show significantly higher performance compared to published 4130 steel-steel properties. The shear failure



in the builds with interlayers occurred by delamination across multiple layers which lead to increase in the total energy absorption.

Disclosure statement

No potential conflict of interest was reported by the authors.

Funding

Financial support for this project is provided by the Government of Israel, Ministry of Defense [PO No. 444080151] and the member organizations of the Smart Vehicle Concepts Center, a National Science Foundation Industry-University Cooperative Research Center under grant NSF IIP 1738723.

ORCID

M. J. Dapino (D) http://orcid.org/0000-0003-4888-1903 S. S. Babu http://orcid.org/0000-0002-3531-2579

References

- [1] Patterson RA. Fundamentals of explosion welding. ASM Handb. 1993;6:160–164.
- [2] Nandan R, DebRoy T, Bhadeshia HKDH. Recent advances in friction-stir welding - process, weldment structure and properties. Prog Mater Sci. 2008;53: 980 - 1023
- [3] Sridharan N, Norfolk M, Babu SS. Characterization of steel-ta dissimilar metal builds made using very high power ultrasonic additive manufacturing (VHP-UAM). Metall Mater Trans A Phys Metall Mater Sci. 2016;47:2517-2528.
- [4] Sridharan N, Gussev M, Seibert R, et al. Rationalization of anisotropic mechanical properties of Al-6061 fabricated using ultrasonic additive manufacturing. Acta Mater. 2016.
- [5] Wolcott PJ, Sridharan N, Babu SS, et al. Characterisation of Al-Ti dissimilar material joints fabricated using ultrasonic additive manufacturing. Sci Technol Weld Join. [Internet]. 2016;21:114–123. Available from: http://www.tandfonline.com/doi/full/10.1179/13621718 15Y.0000000072.
- [6] Sridharan N, Wolcott P, Dapino M, et al. Microstructure and mechanical property characterisation of aluminium-steel joints fabricated using ultrasonic additive manufacturing. Sci Technol Weld Join. 2016: 1-8.
- [7] Sridharan N, Wolcott P, Dapino M, et al. Microstructure and texture evolution in aluminum and commercially pure titanium dissimilar welds fabricated using ultrasonic additive manufacturing. Scr Mater. [Internet]. 2016;117:1-5. Available from: http://dx.doi.org/ 10.1016/j.scriptamat.2016.02.013.
- [8] Lu Y, Huang JY, Wang C, et al. Cold welding of ultrathin gold nanowires. Nat Nanotechnol. 2010;5:218-224.
- [9] Milner DR, Rowe GW. Fundamentals of solid-phase welding. Metall Rev. 1962;7:433-480.
- [10] Vaidyanath LR, Nicholas MG, Milner DR. Pressure welding by rolling. Br Weld J. 1959;6:13–28.
- [11] Levy A, Miriyev A, Sridharan N, et al. Ultrasonic additive manufacturing of steel: method, post-processing treatments and properties. J Mater Process Technol. 2018;256:183-189.

- [12] Gussev MN, Sridharan N, Norfolk M, et al. Effect of post weld heat treatment on the 6061 aluminum alloy produced by ultrasonic additive manufacturing. Mater Sci Eng A. 2016.
- [13] Gussev MN, Sridharan N, Thompson Z, et al. Influence of hot isostatic pressing on the performance of aluminum alloy fabricated by ultrasonic additive manufacturing. Scr Mater. 2018;145:33–36.
- [14] Sridharan N, Gussev MN, Parish CM, et al. Evaluation of microstructure stability at the interfaces of Al-6061 welds fabricated using ultrasonic additive manufacturing. Mater Charact. 2018;139:249-258.
- [15] Sriraman MR, Babu SS, Short M. Bonding characteristics during very high power ultrasonic additive manufacturing of copper. Scr Mater. [Internet]. 2010;62:560–563. Available from: http://dx.doi.org/10. 1016/j.scriptamat.2009.12.040.
- [16] Truog AG. Bond improvement of Al/Cu joints created by very high power ultrasonic additive manufacturing. The Ohio State University; 2012.
- [17] Schick DE, Hahnlen RM, Dehoff R, et al. Microstructural characterization of bonding interfaces in Aluminum 3003 blocks fabricated by ultrasonic additive manufacturing. Weld J. 2010;89:105-115.
- [18] Uday MB, Ahmad Fauzi MN, Zuhailawati H, et al. Advances in friction welding process: a review. Sci Technol Weld Join. 2010;15:534-558.
- [19] Schick D, Babu S, Foster D. Transient thermal response in ultrasonic additive manufacturing of aluminum 3003. Rapid Prototyp J. 2011;17:369–379.
- [20] Sridharan N, Wolcott P, Dapino M, et al. Microstructure and mechanical property characterisation of aluminium-steel joints fabricated using ultrasonic additive manufacturing. Sci Technol Weld Join. [Internet]. 2017;22:373–380. Available from: https://doi.org/10. 1080/13621718.2016.1249644.
- [21] Sridharan N, Isheim D, Seidman DN, et al. Colossal super saturation of oxygen at the iron-aluminum interfaces fabricated using solid state welding. Scr Mater. 2017;130:196-199.
- [22] Million B, Růžičková J, Velíšek J, et al. Diffusion processes in the Fe-Ni System. Mater Sci Eng. 1981;50: 43 - 52.
- [23] Dean DC, Goldstein JI. Determination of the interdiffusion coefficients in the Fe-Ni and Fe-Ni-P Systems below 900°C. Metall Mater Trans A. 1986;17: 1131-1138.
- [24] Borgenstam A, Engstro A, Ho Lund L, et al. Basic and applied research: section I DICTRA, a tool for simulation of diffusional transformations in alloys. J Phase Equilibria. 2000;21:269-280.
- [25] Andersson JO, Helander T, Höglund L, et al. Thermo-Calc & DICTRA, computational tools for materials science. Calphad. 2002;26:273-312.
- [26] Oliver WC, Pharr GM. An improved technique for determining hardness and elastic modulus using load and displacement sensing indentation experiments. J Mater Res. 1992;7:1564-1583.
- [27] Ivanisenko Y, Lojkowski W, Valiev RZ, et al. The mechanism of formation of nanostructure and dissolution of cementite in a pearlitic steel during high pressure torsion. Acta Mater. 2003;51:5555-5570.
- [28] Takahashi J, Kawakami K, Ueda M. Atom probe tomography analysis of the white etching layer in a rail track surface. Acta Mater. 2010;58:3602-3612.